

**Technical note: A
numerical test-bed
for ice nucleation**

R. J. Cotton et al.

Technical note: A numerical test-bed for detailed ice nucleation studies in the AIDA cloud simulation chamber

R. J. Cotton¹, S. Benz², P. R. Field^{1,*}, O. Möhler², and M. Schnaiter²

¹Met Office, Exeter, Devon EX1 3PB, UK

²Institute for Meteorology and Climate Research, Forschungszentrum Karlsruhe, Germany

*now at: National Center for Atmospheric Research (NCAR), Boulder, CO, USA

Received: 30 August 2006 – Accepted: 18 September 2006 – Published: 27 September 2006

Correspondence to: R. J. Cotton (richard.cotton@metoffice.gov.uk)

Title Page

Abstract

Introduction

Conclusions

References

Tables

Figures

◀

▶

◀

▶

Back

Close

Full Screen / Esc

Printer-friendly Version

Interactive Discussion

Abstract

The AIDA (Aerosol Interactions and Dynamics in the Atmosphere) aerosol and cloud chamber of Forschungszentrum Karlsruhe can be used to test the ice forming ability of aerosols. The AIDA chamber is extensively instrumented including pressure, temperature and humidity sensors, and optical particle counters. Expansion cooling using mechanical pumps leads to ice supersaturation conditions and possible ice formation. In order to describe the evolving chamber conditions during an expansion, a detailed microphysics size-resolving parcel model was modified to account for diabatic heat and moisture interactions with the chamber walls. Model results are shown for a series of expansions where the initial chamber temperature ranged from -20°C to -60°C and which used desert dust as ice forming nuclei. During each expansion, the initial formation of ice particles was clearly observed. For the colder expansions there were two clear ice nucleation episodes.

In order to test the ability of the model to represent the changing chamber conditions and to give confidence in the observations of chamber temperature and humidity, and ice particle concentration and mean size, ice particles were simply added as a function of time so as to reproduce the observations of ice crystal concentration. The time interval and chamber conditions over which ice nucleation occurs is therefore accurately known, and enables the model to be used as a test bed for different representations of ice formation.

1 Introduction

The ice formation mechanism, whether by homogeneous freezing of solution droplets or heterogeneous nucleation on insoluble aerosols, affects the properties of cirrus and mixed-phase clouds. This is because the ice formation mechanism determines the ice particle number concentration which changes the mean size and therefore precipitation, microphysical processes such as aggregation and particle growth, and cloud

Technical note: A numerical test-bed for ice nucleation

R. J. Cotton et al.

Title Page

Abstract

Introduction

Conclusions

References

Tables

Figures

◀

▶

◀

▶

Back

Close

Full Screen / Esc

Printer-friendly Version

Interactive Discussion

radiative properties.

There is evidence that heterogeneous ice nucleation is sometimes the dominant process in cloud formation. Aircraft observations suggest that initial ice formation in mid-latitude cirrus can occur at relative humidities lower than the homogeneous freezing threshold (see [Heymsfield et al., 1998](#)). [Seifert et al. \(2003\)](#) showed that the size distribution of the residual aerosols after cirrus ice crystals have been evaporated was not that expected for homogeneous freezing alone. Aircraft observations of orographic wave clouds have also implied that ice crystals can be initiated by heterogeneous nucleation ([Jensen et al., 1998](#); [Field et al., 2001](#)).

Particles that might initiate ice formation in cirrus clouds include black carbon soot, mineral dust and ammonium sulphate aerosols. Aircraft emissions, fossil fuel and biomass burning are sources of soot, while mineral dust is derived from the Earth's surface. Dust from the Saharan desert advected across the Atlantic was observed to act as ice nuclei in the aircraft campaign CRYSTAL-FACE (Cirrus Regional Study of Tropical Anvils and Cirrus Layers – Florida Area Cirrus Experiment) ([Sassen et al., 2003](#); [DeMott et al., 2003](#); [Cziczo et al., 2004](#)). Analysis of the ice crystal residuals from the aircraft campaign INTACC (Interaction of Aerosol and Cold Clouds) described in [Targino et al. \(2006\)](#) showed that when heterogeneous nucleation was observed, mineral dust was more prevalent. [Roberts and Hallet \(1968\)](#) showed that desert dust can be good deposition nuclei.

When the dust particle is coated with soluble material, ice crystals can be initiated by immersion freezing. [Zuberi et al. \(2002\)](#) investigated the effect on the freezing of aqueous ammonium sulphate drops which contained large amounts of insoluble mineral dust. The drops were in the range 10–55 µm diameter and the dust particles were internally mixed throughout the drop volume, with dust concentrations from 10–45% by weight. They found that the drops froze at warmer temperatures and at lower ice super-saturations than the homogeneous freezing of the pure aqueous ammonium sulphate drops. [Kärcher and Lohmann \(2003\)](#) developed a parametrisation of cirrus cloud formation by heterogeneous nucleation and considered possible ice nuclei properties.

Technical note: A numerical test-bed for ice nucleation

R. J. Cotton et al.

Title Page

Abstract

Introduction

Conclusions

References

Tables

Figures

◀

▶

◀

▶

Back

Close

Full Screen / Esc

Printer-friendly Version

Interactive Discussion

They concentrate on immersion freezing as the dominant heterogeneous nucleation mode for cirrus formation at cold temperatures (<235 K).

There are many observations of ice formation in regions where cloud drops are evaporating (Hobbs and Rango, 1985; Cooper, 1995; Field et al., 2001; Baker and Lawson, 2006). A model study of the ice nucleation characteristics of an isolated wave cloud from the INTACC campaign (Cotton and Field, 2002) showed that the observed ice was initiated coincident with the droplet evaporation, rather than from deposition nucleation or homogeneous freezing. Contact nucleation enhanced by the thermophoretic effect of rapidly evaporating droplets has been suggested as responsible for this “evaporation freezing”. Durant and Shaw (2005) hypothesize that the evaporation freezing is due to the freezing temperature of an evaporating drop increasing when the surface of an evaporating drop contacts with an immersed ice nucleus – “contact nucleation inside-out”.

The heterogeneous ice nucleating ability of desert dust samples was investigated in the AIDA (Aerosol Interactions and Dynamics in the Atmosphere) aerosol and cloud chamber. This allows the aerosol concentration and size distribution, and the ambient temperature, pressure, humidity and rate of cooling to be controlled and made similar to upper troposphere conditions. In order to describe the evolving chamber conditions during an expansion, a detailed microphysics size-resolving parcel model was modified to account for diabatic heat and moisture interactions with the chamber walls. Haag et al. (2003) has also described numerical simulations of homogeneous freezing processes in the AIDA chamber, but with simplifications such as partitioning the water between gas and condensate phase according to observations. Firstly, ice particles are added to the model as a function of time so as to reproduce the observations of ice crystal concentration. The agreement between the model and the observations of chamber relative humidity and temperature, and of the ice particle concentration and average diameter improves the confidence in these measurements and in the estimates of the wall fluxes of heat and water vapour. The time interval and chamber conditions over which ice nucleation occurs is therefore accurately known. By estab-

Technical note: A numerical test-bed for ice nucleation

R. J. Cotton et al.

Title Page

Abstract

Introduction

Conclusions

References

Tables

Figures

⏪

⏩

◀

▶

Back

Close

Full Screen / Esc

Printer-friendly Version

Interactive Discussion

lishing the ability of the model to describe the evolving chamber conditions, it can then be used as a test bed for different representations of heterogeneous ice nucleation. Ice particles can then be initiated by means of explicit nucleation acting on aerosol, in order to determine whether or not the simulated process is consistent with the observations.

In Sect. 2 the operation of the AIDA aerosol and cloud chamber is described. Section 3 describes the chemical composition and size distribution of the desert dust samples. Section 4 describes the instrumentation that is used in this study. Section 5 describes the microphysics model with wall heat and vapour fluxes. Section 6 presents a series of observations together with the model results, a summary of the chamber conditions for which the ice particles are initiated, and a discussion of the possible ice nucleation mechanisms. The conclusions are then in Sect. 7.

2 The AIDA chamber and the experimental procedure

A detailed description of the AIDA chamber, the instruments, and the experimental procedure are described in Möhler et al. (2003). AIDA is a large cylindrical chamber made of 2 cm thick aluminium walls, within a thermally isolated containment. The chamber is 7 m high, has a diameter of 4 m and a volume of 84 m³. The interior of the containment can be cooled and maintained to any temperature between ambient and -90°C by ventilation of air cooled in heat exchangers. This containment defines the initial temperature in the aerosol chamber. A fan within the chamber achieves a well-mixed environment where the inhomogeneity in temperature is less than ±0.2 K and the humidity variability is less than ±3%. The chamber pressure is controlled by two large mechanical pumps.

Typically the chamber is operated so that there are several ice nucleation experiments during the day, each using the same aerosol sample. First, the chamber is cleared of any aerosols from previous experiments by pumping down to below 1 hPa and flushed with dry synthetic particle free air. A controlled amount of water vapour is then added to the evacuated chamber which is then filled with dry synthetic air to

Technical note: A numerical test-bed for ice nucleation

R. J. Cotton et al.

Title Page

Abstract

Introduction

Conclusions

References

Tables

Figures

◀

▶

◀

▶

Back

Close

Full Screen / Esc

Printer-friendly Version

Interactive Discussion

Technical note: A numerical test-bed for ice nucleation

R. J. Cotton et al.

Title Page

Abstract

Introduction

Conclusions

References

Tables

Figures

◀

▶

◀

▶

Back

Close

Full Screen / Esc

Printer-friendly Version

Interactive Discussion

atmospheric pressure. This leads to an aerosol background concentration of less than 0.1 cm^{-3} . The chamber is then cooled slowly to the experiment starting temperature using the thermal containment heat exchangers. Once the gas temperature falls below the frost point, water vapour deposits onto the chamber walls. The ice coating on the chamber walls means that the vapour pressure immediately next to the wall is the ice saturation vapour pressure. Heat sources in the chamber mean that the gas temperature is slightly higher than the wall temperature, and therefore all experiments start at just below ice saturation. This ice coating is not uniform over all the chamber walls. Expansion cooling using mechanical pumps then leads to ice supersaturation conditions. The pumping rate can be varied, but typically the pressure is reduced from 1000 hPa to 800 hPa over a few minutes. The equivalent ascent rates, from 1 ms^{-1} to 10 ms^{-1} , are typical of both orographic wave clouds and the convective updrafts measured in cirrus generating cells. Even higher rates of expansion cooling can be reached for short time periods by expansion into an evacuated volume of about 4 m^3 . (The expansions 19–21 reach 20 ms^{-1} as shown in Table 1.) The first expansion is carried out with no aerosol sample in the chamber in order to characterise the background conditions. After adding the aerosol sample, the number concentration and size distribution is measured using standard aerosol instrumentation.

The cooling rate deviates from that expected if the expansion was adiabatic. (See Möhler et al. (2005) for a discussion of the heat fluxes.) This is caused by the increasing heat flux from the 2 cm thick aluminium chamber walls. Figures 1a and 1b shows the chamber pressure and the resultant cooling for an example chamber expansion. The equivalent updraft of an adiabatic air parcel undergoing the chamber cooling rate is also shown, and is given by,

$$w = -\frac{C_p}{g} \frac{dT_g}{dt} \quad (1)$$

where T_g is the chamber bulk gas temperature. The updraft, w , is used to force the parcel model. The wall temperature remains approximately constant during the pumping due to the large heat capacity of the chamber walls. Eventually the gas temperature

reaches an equilibrium value where the expansion cooling and the heat flux from the warmer walls balance.

During the expansion cooling there is also a water vapour flux from the ice coated chamber walls into the gas volume. For some expansions, the change in total mixing ratio is comparable to the condensate mixing ratio, (Fig. 1c). Because the wall temperature is always almost constant during the expansions, the water vapour pressure above the ice-coated chamber walls is also constant. The vapour pressure in the bulk gas, however, is reduced by the decreasing pressure and temperature during the expansion. Once liquid or ice particles are formed, the particle diffusional growth also reduces the bulk gas water vapour pressure. This varying difference in vapour pressure leads to a water vapour flux from the chamber walls to the bulk gas. During the chamber expansion the total water mixing ratio is therefore not constant.

3 Aerosol description

Two dust samples were collected from the ground, in the Takla Makan desert in China (referred to as Asian dust AD1) and north of Cairo city (Saharan dust SD2). The details of the elemental composition and aerosol size spectra are in Möhler et al. (2006). X-ray fluorescence analysis showed that silicon, aluminium and calcium oxides were abundant. The aerosols which were added to the chamber were selected by dry dispersion of the dust samples and inertial removal of particles greater than 2 µm diameter. The size distributions of the aerosols were approximately log-normal with a range between 0.1 and 2 µm, mode diameter of 0.3 to 0.5 µm and standard deviation of 1.6 to 1.9.

4 Instrumentation

The AIDA chamber is extensively instrumented including pressure, temperature and water vapour sensors, and optical particle counting probes and aerosol characterisation devices (see Möhler et al., 2003 and Möhler et al., 2005). The gas and chamber

Technical note: A numerical test-bed for ice nucleation

R. J. Cotton et al.

Title Page

Abstract

Introduction

Conclusions

References

Tables

Figures

◀

▶

◀

▶

Back

Close

Full Screen / Esc

Printer-friendly Version

Interactive Discussion

wall temperatures are measured with an array of platinum resistance thermometers and thermocouples. The variation between all measured temperatures is less than ± 0.3 K. The instruments used in this study are the total water and water vapour sensors, aerosol characterisation and the small ice detector (SID).

5 4.1 Total water mixing ratio

A chilled mirror hygrometer (MBW) measures the frost point. The chamber air is sampled through a heated tube so that any ice or liquid particles are rapidly evaporated and hence this instrument can be used to measure the total water mixing ratio in the chamber. The sampling efficiency is estimated to be 100% for ice and liquid particles below $7 \mu\text{m}$ diameter. The total water mixing ratio is therefore less reliable when there are larger particles at high concentrations. The frost point accuracy is estimated to be ± 0.1 K.

4.2 Water vapour

The water vapour pressure inside the chamber is directly measured by a tunable diode laser (TDL) hygrometer. In order to significantly reduce systematic errors caused by uncertainties in the absorption lines, the TDL is corrected by comparison with the cooled mirror hygrometer prior to each expansion. The estimated error is $\pm 1.3\%$ at 220 K to $\pm 1.7\%$ at 190 K, which for the ice saturation ratio is $\pm 4.0\%$ at 220 K and $\pm 6\%$ at 190 K. For this study, the TDL water vapour is used only as a consistency check after the model has run. In future studies, the corrected TDL water vapour might be used directly as an input to the model, similar to how the pressure is used.

4.3 Aerosols

The aerosol number concentration is measured by a condensation particle counter (CPC) where particles less than $2 \mu\text{m}$ diameter are sampled with 100% efficiency. Ice particles that are formed during the chamber expansion evaporate in the warm sample

Technical note: A numerical test-bed for ice nucleation

R. J. Cotton et al.

Title Page

Abstract

Introduction

Conclusions

References

Tables

Figures

◀

▶

◀

▶

Back

Close

Full Screen / Esc

Printer-friendly Version

Interactive Discussion

tube. When the ice particles are formed on insoluble aerosols, the residual after evaporation can enter the CPC. The non-quantified size dependent loss in the sampling tube, however, means that the total aerosol concentration when there are ice particles present has a large error.

5 4.4 Small particle phase, size and concentration

Particle concentrations and mean particle size are measured using a laser scattering device, the small ice detector (SID), described by [Hirst et al. \(2001\)](#). The SID can count and size particles above 1 μm diameter and discriminate between liquid water drops and ice particles. The probe has six photo-detectors arranged azimuthally at a 30° forward scattering angle. One photo-detector acts as a trigger, and the variation in the signals from the other five photo-detectors is used to determine the particle phase. The photo-detector signal variation is specified by an asphericity factor, A_f , defined by

$$A_f = k \frac{\sqrt{\sum_{i=1,5} (\langle E \rangle - E_i)^2}}{\langle E \rangle} \quad (2)$$

where E_i is the i 'th photo-detector signal, and k is a constant set so that A_f is in the range 0–100. Spherical liquid water drops scatter the laser uniformly in azimuth and therefore should give a low asphericity value. Ice particles, which are non-spherical, scatter the laser non-uniformly and therefore give a high asphericity. A nominal threshold of $A_f=12$ is chosen (this allows good discrimination between liquid water drops and ice particles from in-situ aircraft observations in Stratocumulus and Cirrus clouds).

The particle radius, R , is derived from the mean photo-detector signal using the power law,

$$R = a \langle E \rangle^{0.51} \quad (3)$$

where a is estimated by comparing the measured bulk liquid water content obtained with hot wire probes in Stratocumulus cloud with that obtained by the SID. The SID size estimation is therefore only correct for spherical liquid droplets.

Technical note: A numerical test-bed for ice nucleation

R. J. Cotton et al.

Title Page

Abstract

Introduction

Conclusions

References

Tables

Figures

◀

▶

◀

▶

Back

Close

Full Screen / Esc

Printer-friendly Version

Interactive Discussion

Technical note: A numerical test-bed for ice nucleation

R. J. Cotton et al.

Title Page

Abstract

Introduction

Conclusions

References

Tables

Figures

◀

▶

◀

▶

Back

Close

Full Screen / Esc

Printer-friendly Version

Interactive Discussion

Because of the detector noise, not all small ice particles have an asphericity above the $A_f=12$ threshold. This is shown in Fig. 2 which is one of the coldest expansions using Saharan desert dust where the chamber gas temperature decreased from -60°C to -65°C . In Fig. 2a, the solid line at $A_f=12$ is drawn to separate the non-spherical from the spherical particles. The particle diameters in Fig. 2b show the ice crystals being initiated between about 30 and 160 s. The SID particle diameter is only calibrated for spherical particles, but does indicate the trend towards increasing non-spherical particle diameter. In Fig. 2c, the histogram of A_f for the particles sampled after 200 seconds, shows that around 70% of the small ice particles are classified as non-spherical. In the modelling studies described here, the SID non-spherical concentration is therefore increased by a factor of 1.4.

5 Parcel model with heat and vapour fluxes

The parcel model is a detailed microphysics size-resolving model modified to include heat and vapour fluxes from the chamber walls. The unmodified parcel model (described in detail in Cotton and Field (2002)) considers an adiabatic parcel of air containing a conserved mass of water being lifted by a variable updraft. The parcel model was also used in the Cirrus Parcel Model Comparison (CPMC) project as part of the GEWEX Cloud System Studies on cirrus clouds (GCSS WG2) which compared results from various parcel models over a range of updraft velocities and CCN spectrum (see Lin et al., 2002).

For the model initialisation, we simply assume that all the aerosol measured in the AIDA chamber using the CPC can act as CCN. The dry CCN size spectrum was log-normally distributed between 0.1 and 2.0 μm diameter, with a mode of 0.4 μm , with the total concentration given by the initial CPC aerosol concentration. The CCN were only important for expansions 18–21 (listed in Table 1) where liquid drops were observed before any ice particles.

5.1 Wall heat flux

The wall heat flux contributes to the rate of change of gas temperature. The heat flux diabatic term is assumed to be proportional to the temperature difference between the gas and chamber wall,

$$\frac{dT_g}{dt} \Big|_{\text{wallflux}} = \frac{K_T}{C_p} [T_w - T_g] \quad (4)$$

where K_T is simply chosen on an expansion by expansion basis to give the best fit to the gas temperature. The detailed physics of the heat flux is contained within K_T . Fig. 3 shows the K_T term for each expansion. The horizontal error bar represents the range of temperature observed during the expansion, the vertical bar is the estimated error on K_T . There is a good correlation of K_T with temperature.

5.2 Wall water vapour flux

The water vapour flux contributes to the rate of change of total water mixing ratio, q_T . The water vapour flux can be included in different ways. The first is analogous to the formulation of the wall heat flux, i.e. the vapour flux is proportional to the difference in vapour pressure just above the chamber wall and in the bulk gas,

$$\frac{dq_T}{dt} \Big|_{\text{wallflux}} = K_V \frac{0.622}{P \rho_{\text{air}}} [e_{s,i}(T_w) - \sigma_i e_{s,i}(T_g)] \quad (5)$$

where K_V is a constant, $e_{s,i}$ is the ice saturation vapour pressure and σ_i is the ratio of the ice vapour pressure in the bulk gas to the ice saturation vapour pressure. Because the wall temperature, T_w , is always almost constant during the expansions when the chamber wall is completely ice-coated, the saturation vapour pressure, $e_{s,i}(T_w)$, is also constant. This parametrisation does not work well for all chamber expansions.

A second approach is to calculate the vapour flux from the heat flux assuming a boundary layer. This will be expanded further in a later paper.

Title Page

Abstract

Introduction

Conclusions

References

Tables

Figures

◀

▶

◀

▶

Back

Close

Full Screen / Esc

Printer-friendly Version

Interactive Discussion

An alternative approach to parametrising the wall vapour flux is to assume that the MBW hygrometer measures the chamber total water mixing ratio accurately. This is reasonable since significant errors are expected only with the presence of large ice particles, and for all the chamber expansions shown here, only small particles are observed. The model is constrained by the measured total water content at each time-step during the expansion. Any differences in ice concentration between model and chamber will result in a different partitioning of the total water between ice and vapour. This will in turn be manifested as a difference between the model vapour mixing ratio and that measured by the TDL. For only some of the expansions, each water vapour flux method gives similar results. The reason for the discrepancy between the different methods for most of the expansions is due to the fact that the ice layer on the chamber walls is not uniform and that not all the chamber surface is covered with ice. The third method is used for the results described here.

5.3 Ice initiation method

In order to test the ability of the model to reproduce the observations, ice particles may be added to the model as a function of time so as to reproduce the SID particle number concentration (scaled by 1.4), rather than initiating ice particles by means of explicit nucleation acting on aerosol. The ice particles are initiated in the smallest ice particle size bin ($0.1 \mu\text{m}$). When run in this way, the model is then providing a test of the assumptions used within it which determine the diffusional growth rate of ice. These include the crystal capacitance and the water vapour accommodation coefficient. If these parameters were grossly in error, the model would not reproduce the observed water vapour evolution even when constrained to the observed total water and ice initiation.

Technical note: A numerical test-bed for ice nucleation

R. J. Cotton et al.

Title Page

Abstract

Introduction

Conclusions

References

Tables

Figures

◀

▶

◀

▶

Back

Close

Full Screen / Esc

Printer-friendly Version

Interactive Discussion

6 Observations and model results

Table 1 lists some details of the chamber expansions for both dust samples, with the chamber temperature covering a range of -20°C to -65°C . The expansions are divided into four temperature regimes. For the first, regime I (expansions 44–45) only one nucleation mode is observed, while for regimes II and III (expansions 26–42 and 22–25) two separate nucleation modes are generally observed. The last, regime IV (expansions 18–21) reaches water saturation, and liquid water is observed.

Figures 4–7 show the modeled and observed data from example chamber expansions, one from each of the four temperature regimes. Panel (a) shows the chamber pressure and equivalent updraft. In all cases, the start of the expansion is at zero seconds. Prior to this, the pressure decreases very slowly due to the continuous sample flow through the particle probes. The pressure change has been converted into an updraft assuming adiabatic expansion in order to force the parcel model. The pumping rate during each expansion was often varied, giving a step-change in the equivalent updraft. Panel (b) shows the chamber bulk gas and wall temperatures. The wall temperature is constant but the bulk gas temperature deviates from that expected if the expansion was adiabatic because of the significant wall to bulk gas heat flux. However, the modeled gas temperature (the thicker grey line) using a parametrised heat flux with a constant K_7 as defined by Eq. (4) enables a good match with the observations. Panel (c) shows the mass mixing ratio of the total water content (measured using the MBW) and the total condensate mixing ratio calculated as the difference between the total and water vapour mixing ratio (measured using the TDL). The model is constrained to follow exactly the total water content measurement. The pressure (and hence updraft), temperature and total water mixing ratio have been adjusted to fit, so there is no surprise about the good agreement. The condensate mixing ratio depends, however, on the validity of the model microphysics. Panel (d) shows the observed and modeled relative humidity w.r.t. ice, RH_{ice} , and w.r.t. water, RH_{water} . The agreement with the TDL derived humidity is confirmation that the model correctly partitions the water be-

Technical note: A numerical test-bed for ice nucleation

R. J. Cotton et al.

Title Page

Abstract

Introduction

Conclusions

References

Tables

Figures

◀

▶

◀

▶

Back

Close

Full Screen / Esc

Printer-friendly Version

Interactive Discussion

tween vapour and condensate. The chamber humidity starts just below ice saturation because of heat sources within the bulk gas (mainly mixing fans). For some expansions the chamber walls were not coated in ice and the initial humidity starts much lower than ice saturation. Panel (e) shows the measured asphericity factor, A_f , of all particles sampled by the SID. The line $A_f=12$ is drawn to separate the non-spherical from the spherical particles. Panel (f) shows the SID particle diameter together with the modeled mean diameter (thick grey line). The SID particle diameter is only correct for spherical particles, but does indicate the trend towards increasing non-spherical particle diameter. Panel (g) shows the SID particle concentrations, for non-spherical ($A_f>12$, solid line) and for all particles (dashed line), averaged over 10 second time-intervals. The modeled ice particle concentration, where the diameter is greater than $3\ \mu\text{m}$ (which is the estimated SID threshold) and for all sizes, are shown by the two thick grey lines.

The onset and duration of ice nucleation is estimated from the broad swath of SID particle diameters and from the SID non-spherical particle concentration. The light grey vertical shading just indicates this ice particle initiation time interval. If there is also a second distinct ice nucleation mode, this is indicated by a darker grey band. The ice nucleation scheme in the model simply initiates ice particles at a constant rate, shown in panel (g) (thick grey lines) through this time interval, so that at the end the ice crystal concentration matches the SID non-spherical particle concentration scaled by 1.4 (as listed in Table 1). Panel (h) shows the evolution of RH_{ice} with temperature during the cooling (expansion) phase. The thick grey shading on the curve indicates the period when ice crystals are added to the model. The model temperature and humidity is used because of uncertainties in the measured humidity.

6.1 Temperature regime I: single nucleation mode

Figure 4 shows the coldest expansion using Saharan desert dust (Expansion 45) where the chamber gas temperature decreased from -60°C to -65°C . At 200 s, the pumping rate is reduced leading to a reduction in the equivalent updraft from 3 to $2.5\ \text{ms}^{-1}$.

Technical note: A numerical test-bed for ice nucleation

R. J. Cotton et al.

Title Page

Abstract

Introduction

Conclusions

References

Tables

Figures

◀

▶

◀

▶

Back

Close

Full Screen / Esc

Printer-friendly Version

Interactive Discussion

Technical note: A numerical test-bed for ice nucleation

R. J. Cotton et al.

Before 30 seconds, most particles are less than $3\ \mu\text{m}$ diameter with $A_f < 12$, and are larger introduced aerosol particles. The broad swath of particle diameters in panel (f) coincident with $A_f > 12$ indicates that ice particles are being initiated between 30 and 160 s. The increasing particle diameter trend is modelled well. However up to 300 s, the model overestimates RH_{ice} and underestimates the condensate mass mixing ratio. Since the model total water mixing ratio is constrained to follow the measured values (from the MBW), this suggests that the model ice crystals are growing too slowly after nucleation. This leaves excess water substance in the vapour phase and insufficient condensate. This can result from errors in key factors that control depositional growth rate, such as the ice crystals capacitance and deposition coefficient.

6.2 Temperature regime II: two ice nucleation modes

Figure 5 shows the expansion using Asian desert dust (Expansion 28) where the chamber gas temperature decreased from -50°C to -57°C . The chamber pumping rate is now constant throughout the expansion and the maximum relative humidity is reached before the expansion pumping stops. Ice crystal depositional growth causes the chamber humidity to decrease at 260 s. The SID probe asphericity factor A_f (panel e) and estimated diameter (panel f) indicate two distinct ice nucleation modes. The first nucleation mode occurs near the start of the expansion pumping, where conditions are just above ice saturation and is indicated by the light grey vertical shading. The second nucleation mode occurs later, but still below water saturation and is indicated by the dark grey vertical shading. Early, during the ice crystal growth phase, the modelled relative humidity agrees well with the observations, and only when the ice crystals begin to evaporate does the humidity diverge. This is the third in a series of expansions during one day using the same aerosol sample. In the next (expansion 29) there is a more obvious separation between the nucleation modes and in the earlier expansion 27 the modes overlap.

[Title Page](#)[Abstract](#)[Introduction](#)[Conclusions](#)[References](#)[Tables](#)[Figures](#)[◀](#)[▶](#)[◀](#)[▶](#)[Back](#)[Close](#)[Full Screen / Esc](#)[Printer-friendly Version](#)[Interactive Discussion](#)

6.3 Temperature regime III: two nucleation modes

Figure 6 shows the expansion using Asian desert dust (Expansion 24) where the chamber gas temperature decreased from -35°C to -45°C . The pumping rate leads to an equivalent updraft of around 6 m s^{-1} . Similar to expansion 28 from temperature regime II, the SID asphericity and diameter imply two ice nucleation modes. The first nucleation mode occurs near the start of the expansion pumping, where conditions are just above ice saturation and is indicated by the light grey vertical shading, while the second nucleation mode occurs later, but still below water saturation and is indicated by the dark grey vertical shading.

6.4 Temperature regime IV: one nucleation mode, liquid water observed

Figure 7 shows the expansion using Asian desert dust (Expansion 19) where the chamber gas temperature decreased from -20°C to -32°C . This expansion reaches water saturation and both water drops and ice particles are observed. The chamber pumping rate is very fast and the equivalent updraft is around 10 m s^{-1} . The SID asphericity and diameter show that between 110 and 170 s the chamber is dominated by spherical water drops. At 110 s the chamber reaches water saturation as shown in panel (d). The SID asphericity and diameters also indicate that ice particles are present during this liquid dominated interval. The ice particles are produced at some time during this liquid dominated interval, not before. Any deposition ice nuclei would likely activate during this ice supersaturated period.

6.5 Ice nucleation characteristics of all chamber expansions

Figure 8 shows the changing environmental conditions inside the chamber and highlights when the ice nucleation is occurring (as for panel (h) in the earlier figures) for all the expansions in each of the four temperature regimes. Each line represents the model humidity and temperature, rather than the measured values. The range over

Title Page

Abstract

Introduction

Conclusions

References

Tables

Figures

◀

▶

◀

▶

Back

Close

Full Screen / Esc

Printer-friendly Version

Interactive Discussion

which the first nucleation mode occurs is shown by the thicker light-grey line, the second mode by the dark-grey line. Also shown are lines which characterise homogeneous freezing and immersion freezing parametrisations. The homogeneous freezing lines use the [Koop et al. \(2000\)](#) water activity parametrisation. The lines show the critical humidity at which half the drops freeze in 10 s, for a radius of 0.5 and 5 μm assuming ammonium sulphate. The dashed line is from [Zuberi et al. \(2002\)](#) and is the critical ice saturation for freezing of ice in aqueous ammonium sulphate drops with kaolinite and montmorillonite dust inclusions.

Expansions in each of the temperature regimes show different ice nucleation modes. The cold expansions in temperature regimes II and III ($-60^{\circ}\text{C} < T_g < -40^{\circ}\text{C}$), typically show two ice nucleation modes active over different time intervals. The first nucleation mode starts at low ice supersaturations and may be deposition nucleation. The second mode may also be deposition nucleation onto a subset of the dust particles, or if there is a soluble component forming on the aerosols, immersion or homogeneous freezing. The critical humidity lines in Fig. 8 representing homogeneous freezing and immersion freezing indicate that this second ice nucleation mode is probably the latter. The warm expansions in temperature regime IV ($T_g > -35^{\circ}\text{C}$), show no ice crystals are initiated before liquid water droplets are formed. The ice nucleation mode is immersion or condensation freezing. The coldest expansions in temperature regime I ($T_g < -60^{\circ}\text{C}$) show only one ice nucleation mode which starts at low ice supersaturation and is probably deposition nucleation.

The expansions 22–24 (Asian dust AD1) and 40–41 (Saharan dust SD2) show that the onset of ice nucleation occurs at lower relative humidity for each successive expansion. The expansions 26–29 (Asian dust AD1) show an increased separation between the ice nucleation modes for each successive expansion. During these expansions, there is aerosol processing with the ice forming nuclei being conditioned in some way to nucleate at lower relative humidities after each evaporation.

Technical note: A numerical test-bed for ice nucleation

R. J. Cotton et al.

Title Page

Abstract

Introduction

Conclusions

References

Tables

Figures

◀

▶

◀

▶

Back

Close

Full Screen / Esc

Printer-friendly Version

Interactive Discussion

6.6 Sensitivity of the model-observation agreement to different ice nucleation parametrisations

What is the sensitivity of the model-observation agreement to different more “physically-based” ice nucleation parametrisations? Figure 9 shows models results for expansion 23 where the chamber temperature starts at -35°C and reaches -43°C as water saturation is approached. The first ice nucleation mode, which starts just above ice saturation is parametrised as before, by just inserting ice particles to match the SID observations. The second ice nucleation mode, which occurs near water saturation is parametrised as homogeneous freezing following Koop et al. (2000). It is simply assumed that a subset of the aerosols can form solution droplets and that when dry, have a similar size distribution to the observed aerosol (log-normal with a range between 0.1 and $2\ \mu\text{m}$, mode diameter of $0.4\ \mu\text{m}$ and standard deviation of 1.7) The solute is assumed to be either ammonium sulphate or sulphuric acid and the ice crystal capacitance 1.0 or 0.8. In each case, the subset fraction is just set so as to give the observed final ice concentration. In all cases, the modelled relative humidity compares well with that given by the TDL, except for perhaps a 5% discrepancy near the peak humidity. The SID particle average diameter and concentration show in more detail how the homogeneous freezing parametrisation fails. As discussed earlier, the SID size estimation is only calibrated for liquid water drops but it does show the general size increase. While the onset of freezing agrees, the observations show freezing occurring over a much wider time interval. There is little difference in the freezing rate when either ammonium sulphate or sulphuric acid is used. At some point during the freezing, the rapidly growing of ice crystals deplete the ambient humidity and stop further freezing. The final ice crystal concentration is very sensitive to the freezing rate and the ice crystal growth rate (which is affected by the capacitance factor). However, the unknown subset fraction was arbitrarily set, so the final ice crystal concentration will not give any information regarding the freezing process.

Figure 10 shows models results for expansion 44 where the chamber temperature

Technical note: A numerical test-bed for ice nucleation

R. J. Cotton et al.

Title Page

Abstract

Introduction

Conclusions

References

Tables

Figures

⏪

⏩

◀

▶

Back

Close

Full Screen / Esc

Printer-friendly Version

Interactive Discussion

starts at -60°C and the relative humidity does not reach the homogeneous freezing threshold. There is only one clear ice nucleation mode, which starts just above ice saturation. The brown and red lines are for models parametrising deposition nucleation following Meyers et al. (1992) where the number of ice nuclei are increased (by a factor of 1000) to give the observed final ice concentration. This increase is just because the initial aerosol concentration that is inserted into the chamber is not representative of the atmosphere. The difference between these models is the value of the ice crystal capacitance ($C=1$ for the brown line, and $C=0.8$ for the red). Decreasing the capacitance slows the ice crystal growth, enabling higher ambient humidities, which in turn leads to higher ice crystal concentrations. The relative humidity rises above what is observed. This might suggest that the depositional growth rate in the model is too small (and could be increased by changing the capacitance value or the accommodation coefficient). However, the unknown scale factor was arbitrarily set, so the final ice crystal concentration will not give any information regarding the capacitance. The mustard line represents the model when ice nucleation is parametrised following Möhler et al. (2006) which fits the observed nucleation rate to

$$\frac{dn_{\text{ice}}}{dt} = n_a a \frac{dS_i}{dt} \quad (6)$$

where n_a is the aerosol particle concentration, S_i is the ice relative humidity and a is a fit parameter. This nucleation is only active above some threshold ice relative humidity S_0 . For expansion 44, $a=1.7$ and $S_0=1.0$. This gives a much better fit to the relative humidity, mean particle diameter and ice crystal concentrations. The ability to discriminate between different ice nucleation parametrisations is also dependant on knowing the SID ice crystal size threshold. Figure 10c shows, for each model run, two concentrations. One is for all ice crystals and the other for ice crystals greater than $3\mu\text{m}$ diameter. The low temperatures and therefore low crystal growth rates for this expansion, means that the uncertainty in SID size threshold affects the discrimination much more than the warmer, more humid homogeneous freezing expansion 23.

Technical note: A numerical test-bed for ice nucleation

R. J. Cotton et al.

Title Page

Abstract

Introduction

Conclusions

References

Tables

Figures

◀

▶

◀

▶

Back

Close

Full Screen / Esc

Printer-friendly Version

Interactive Discussion

7 Conclusions

The AIDA cloud simulation chamber enables the onset of ice nucleation to be clearly observed (as shown in Haag et al. , 2003 and Field et al. , 2006). Desert dust samples from Sahara and Asia were tested in multiple chamber expansions between -20°C and -60°C . The ice nucleation characteristics were varied. For many expansions, two separate ice nucleation events were observed, while for the warmest expansions, no ice crystals were initiated before liquid water droplets were formed. A parcel model which incorporates heat and water vapour flux from the chamber wall into the bulk gas was developed to give confidence to the measured particle concentrations and chamber humidity and temperature. The heat flux is a simple parametrisation while the water flux uses the measured total water as a constraint. The model then partitions the water between vapour and condensate according to microphysics assumptions. In order to test the self-consistency of the observations and to better determine the relative humidity, ice particles were added to the model as a function of time so as to reproduce the SID particle number concentration, rather than initiating ice particles by means of explicit nucleation acting on aerosol. The model reproduces the observations for all expansions very well. The temperature and relative humidity conditions over which ice nucleation is occurring and the number concentration and size of ice crystals are all well specified.

Future work will include running the model with improved ice nucleation parametrisations developed from these and later measurements. The later measurements include the ice nucleating ability of dust particles with soluble coating. For these later measurements, a new version of the SID probe with lower noise and better shape discrimination will be used.

Technical note: A numerical test-bed for ice nucleation

R. J. Cotton et al.

Title Page

Abstract

Introduction

Conclusions

References

Tables

Figures

◀

▶

◀

▶

Back

Close

Full Screen / Esc

Printer-friendly Version

Interactive Discussion

References

- Baker, B. A. and Lawson, R. P.: In situ observations of the microphysical properties of wave, cirrus and anvil clouds. Part 1: Wave clouds, *J. Atmos. Sci.*, in press, 2006. [9486](#)
- Cooper, W. A.: Ice formation in wave clouds: Observed enhancement during evaporation, *Conf. Cloud Physics*, Am. Meteorol. Soc. Dallas, Texas, 147–152, 1995. [9486](#)
- Cotton, R. J. and Field, P. R.: Ice nucleation characteristics of an isolated wave cloud, *Quart. J. Royal Meteorol. Soc.*, 128, 2417–2437, 2002. [9486](#), [9492](#)
- Cziczo, D. J., Murphy, D. M., Hudson, P. K., and Thomson, D. S.: Single particle measurements of the chemical composition of cirrus ice residual during CRYSTAL-FACE, *J. Geophys. Res.*, 109, D04201, doi:10.1029/2003JD004032, 2004. [9485](#)
- DeMott, P. J., Sassen, K., Poellot, M. R., Baumgardner, D., Rogers, D. C., Brooks, S. D., Prenni, A. J., and Kreidenweis, S. M.: African dust aerosols as atmospheric ice nuclei, *Geophys. Res. Lett.*, 30(14), 1732, doi:10.1029/2003GL017410, 2003 [9485](#)
- Durant, A., J. and Shaw, R., A.: Evaporation freezing by contact nucleation inside-out, *Geophys. Res. Lett.*, 32 L20814, doi:10.1029/2005GL024175, 2005 [9486](#)
- Field, P. R., Cotton, R. J., Noone, K., Glantz, P., Kaye, P., Hirst, E., Greenaway, R. S., Jost, C., Gabriel, R., Reiner, T., Andreae, M., Saunders, C. P. R., Archer, A., Choulaton, T., Smith, M., Brooks, B., Hoell, C. Bandy, B., Johnson, D., and Heymsfield, A.: Ice nucleation in orographic wave clouds: Measurements made during INTACC, *Quart. J. Royal Meteorol. Soc.*, 127, 1493–1512, 2001. [9485](#), [9486](#)
- Field, P. R., Möhler, O., Connolly, P., Kraemer, M., Cotton, R., Heymsfield, A. J, Saathoff, H., and Schnaiter, M.: Some ice nucleation characteristics of Asian and Saharan desert dust, *Atmos. Chem. Phys.*, 6, 2991–3006, 2006. [9502](#)
- Jensen, E. J., Toon, O. B., Tabazadeh, A., Sachse, G. W., Anderson, B. E., Chan, K. R., Twohy, C. W., Gandrud, B., Aulenbach, S. M., Heymsfield, A., Hallet, J., and Gary, B.: Ice nucleation processes in upper tropospheric wave-clouds observed during SUCCESS, *Geophys. Res. Lett.*, 25, 1363–1366, 1998 [9485](#)
- Kärcher, B. and Lohmann, U.: A parametrization of cirrus cloud formation: Heterogeneous freezing, *J. Geophys. Res.*, 108, 4402, doi:10.1029/2002JD003220, 2003. [9485](#)
- Koop, T., Luo, B. P., Tsias, A., and Peter, T.: Water activity as the determinant for homogeneous ice nucleation in aqueous solutions, *Nature*, 406, 611–614, 2000 [9499](#), [9500](#), [9514](#)
- Haag, W., Kärcher, B., Schaefers, S., Stetzer, O., Möhler, O., Schurath, U., Krämer, M., and

ACPD

6, 9483–9516, 2006

Technical note: A numerical test-bed for ice nucleation

R. J. Cotton et al.

Title Page

Abstract

Introduction

Conclusions

References

Tables

Figures

◀

▶

◀

▶

Back

Close

Full Screen / Esc

Printer-friendly Version

Interactive Discussion

EGU

- Schiller, C.: Numerical simulations of homogeneous freezing processes in the aerosol chamber AIDA, *Atmos. Chem. Phys.*, 3, 195–210, 2003. [9486](#), [9502](#)
- Heymsfield, A. J., Miloshevich, L. M., Twohy, C., Sachse, G., and Oltmans, S.: Upper tropospheric relative humidity observations and implications for cirrus ice nucleation, *Geophys. Res. Lett.*, 25, 1343–1346, 1998. [9485](#)
- Hirst, E., Kaye, P. H., Greenaway, R. S., Field, P. R., and Johnson, D. W.: Discrimination of micrometre-sized ice and supercooled droplets in mixed phase clouds, *Atmos. Environ.*, 35, 33–47, 2001. [9491](#)
- Hobbs, P. V. and Rango, A. L.: Ice particle concentrations in clouds, *J. Atmos. Sci.*, 42, 2523–2549, 1985. [9486](#)
- Lin, R. L., Starr, D. O., DeMott, P. J., Cotton, R. J., Sassen, K., Jenson, E., Karcher, B., and Liu, X.: Cirrus parcel model comparison project phase 1: The critical components to simulate cirrus initiation explicitly, *J. Atmos. Sci.*, 59(15), 2305–2329, 2002. [9492](#)
- Meyers, M. P., DeMott, P. J., and Cotton, W. R.: New primary ice-nucleation parameterizations in an explicit cloud model, *J. Appl. Meteorol.*, 31, 708–721, 1992. [9501](#), [9516](#)
- Möhler, O., Stetzer, O., Schaefers, S., Linke, C., Schnaiter, M., Tiede, R., Saathoff, H., Kraemer, M., Mangold, A., Budz, P., Zink, P., Schreiner, J., Mauersberger, K., Haag, W., Karcher, B., and Schurath, U.: Experimental investigation of homogeneous freezing of sulphuric acid particles in the aerosol chamber AIDA, *Atmos. Chem. Phys.*, 3, 211–223, 2003. [9487](#), [9489](#)
- Möhler, O., Büttner, C., Linke, C., Schnaiter, M., Saathoff, H., Stetzer, O., Wagner, R., Krmer, M., Mangold, A., Ebert, V., and Schurath, U.: Effect of sulphuric acid coating on heterogeneous ice nucleation by soot aerosol particles, *J. Geophys. Res.*, 110, D11210, doi:10.1029/2004JD005169, 2005 [9488](#), [9489](#)
- Möhler, O., Field, P. R., Connolly, P., Benz, S., Saathoff, H., Wagner, M., Cotton, R., Kraemer, M., Mangold, A., and Heymsfield, A. J.: Efficiency of the deposition mode ice nucleation on mineral dust particles, *Atmos. Chem. Phys.*, 6, 3007–3021, 2006. [9489](#), [9501](#)
- Roberts, P. and Hallet, J.: A laboratory study of the ice nucleating properties of some mineral particulates, *Quart. J. Royal Meteorol. Soc.*, 94, 25–34, 1968. [9485](#)
- Sassen, K., DeMott, P. J., Prospero, J. M., and Poellet, M. R.: Saharan dust storms and indirect aerosol effects on clouds: CRYSTAL-FACE results, *Geophys. Res. Lett.*, 30(12), 1633, doi:10.1029/2003GL017371, 2003. [9485](#)
- Seifert, M., Strom, J., Krejci, R., Minikin, A., Petzold, A., Gayet, J. F., Schumann, U., and Ovar-

Technical note: A numerical test-bed for ice nucleation

R. J. Cotton et al.

Title Page

Abstract

Introduction

Conclusions

References

Tables

Figures

◀

▶

◀

▶

Back

Close

Full Screen / Esc

Printer-friendly Version

Interactive Discussion

- lez, J.: In situ observations of aerosol particles remaining from evaporated cirrus crystals: Comparing clean and polluted air masses, *Atmos. Chem. Phys.*, 3, 1037–1049, 2003. [9485](#)
- 5 Targino, A. C., Krejci, R., Noone, K. J., and Glantz, P.: Single particle analysis of ice crystal residuals observed in orographic wave clouds over Scandinavia during INTACC experiment, *Atmos. Chem. Phys.*, 6, 1977–1990, 2006. [9485](#)
- Zuberi, B., Bertram, A. K., Cassa, C. A., Molina, L. T., and Molina, M. J.: Heterogeneous nucleation of ice in $(\text{NH}_4)_2\text{SO}_4\text{-H}_2\text{O}$ particles with mineral dust immersions, *Geophys. Res. Lett.*, 29(10), 1504, doi:10.1029/2001GL014289, 2002. [9485](#), [9499](#), [9514](#)

Technical note: A numerical test-bed for ice nucleationR. J. Cotton et al.

Title Page

Abstract

Introduction

Conclusions

References

Tables

Figures

◀

▶

◀

▶

Back

Close

Full Screen / Esc

Printer-friendly Version

Interactive Discussion

Table 1. Experiment list grouped into four temperature regimes. The ice concentrations are the SID non-spherical concentration increased by a factor of 1.4. For expansions 27–29, 40–42 and 22–24 there is a second ice initiation phase.

Expansion	Dust sample	Initial aerosol (cm ⁻³)	Equivalent updraft (ms ⁻¹)	K_T ()	First ice nucleation mode		Second ice nucleation mode	
					Temperature (°C)	Ice concentration (cm ⁻³)	Temperature (°C)	Ice concentration (cm ⁻³)
Temperature regime I: Single nucleation mode								
44	SD2	38.4	4.0–3.0,2.5–2.0	3.7	-60.7	42.5		
45	SD2	9.0	4.0–3.0,2.0–2.0	3.7	-60.6	8.7		
Temperature regime II: Two overlapping ice nucleation modes								
26	AD1	99.3	5.2–4.0	3.8	-51.7	21.5		
27	AD1	60.2	5.2–4.0	3.8	-52.0	3.0	-54.6	13.5
28	AD1	36.4	4.0–2.8	3.8	-52.4	1.3	-55.2	4.6
29	AD1	24.1	4.0–2.8	4.1	-52.4	1.1	-55.7	3.8
40	SD2	89.4	4.5–4.0	4.0	-50.8	2.5	-52.4	12.2
41	SD2	53.3	4.0–3.5,2.4–2.3	4.1	-50.9	0.5	-53.1	7.5
42	SD2	32.4	4.0–3.2,2.5–2.3	4.0	-50.6	0.3	-53.6	6.7
Temperature regime III: Two separate ice nucleation modes								
22	AD1	115.9	6.0–4.3	4.3	-39.8	0.5	-40.7	12.0
23	AD1	78.8	6.0–4.2	4.2	-40.2	0.8	-42.2	7.0
24	AD1	56.8	7.0–5.0	4.2	-38.9	1.0	-41.8	12.2
25	AD1	37.3	4.5–3.0	3.9	-39.0	0.5		
Temperature regime IV: Single nucleation mode, Liquid water observed								
18	AD1	180.6	11.0–8.5	4.5	-28.4	10.0		
19	AD1	129.2	20.0,10.0–8.0	4.3	-29.2	10.5		
20	AD1	89.1	20.0,9.5–8.5,1.5–2.0	4.3	-30.9	4.3		
21	AD1	63.8	20.0,9.5–8.5,1.5–2.0	4.4	-31.6	4.0		

Technical note: A numerical test-bed for ice nucleation

R. J. Cotton et al.

Title Page

Abstract

Introduction

Conclusions

References

Tables

Figures

◀

▶

◀

▶

Back

Close

Full Screen / Esc

Printer-friendly Version

Interactive Discussion

**Technical note: A
numerical test-bed
for ice nucleation**

R. J. Cotton et al.

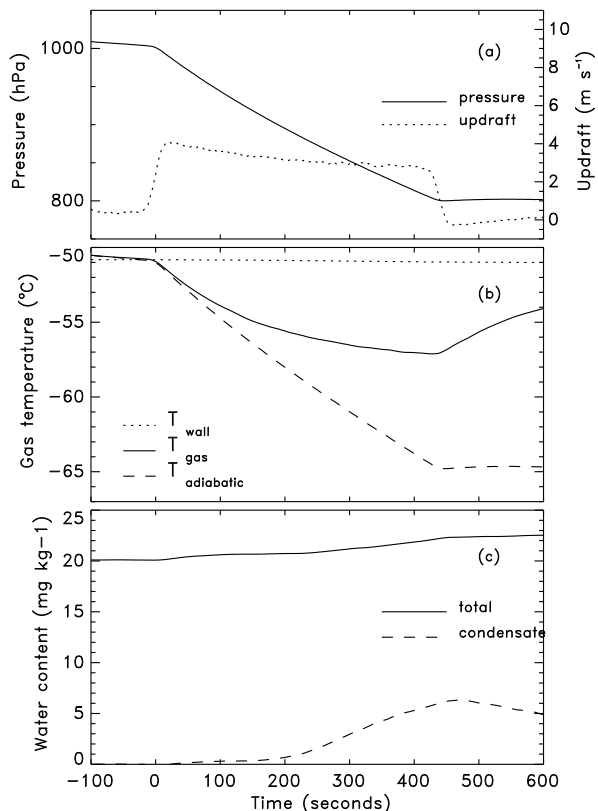


Fig. 1. An example chamber expansion (experiment 28) showing the chamber pressure change (a), and the resultant cooling (b). The effect of the wall vapour flux is shown in panel (c). The time axis is plotted in seconds relative to the start of pumping. There is also a decrease in chamber pressure before the actual expansion starts due to the particle probes sampling the chamber gas.

Title Page

Abstract

Introduction

Conclusions

References

Tables

Figures

◀

▶

◀

▶

Back

Close

Full Screen / Esc

Printer-friendly Version

Interactive Discussion

**Technical note: A
numerical test-bed
for ice nucleation**

R. J. Cotton et al.

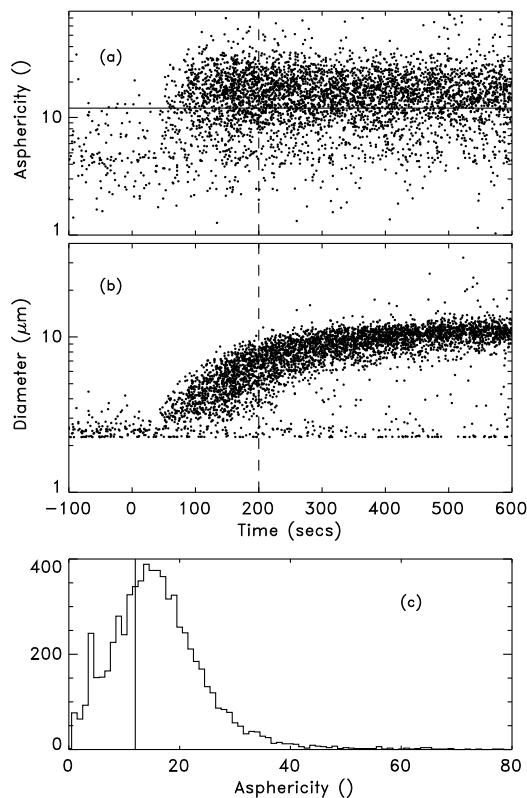
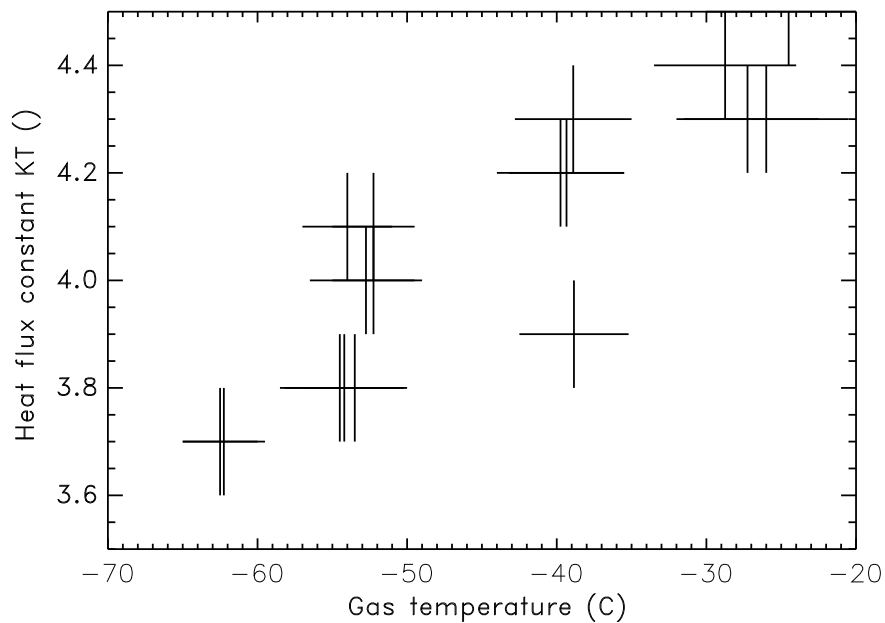


Fig. 2. SID measurements for expansion 45 (Saharan dust, where the chamber gas temperature decreased from -60°C to -65°C). **(a)** shows the asphericity, A_f , for every particle sampled, **(b)** the diameter, and **(c)** a histogram of A_f for particles sampled after 200 s.

[Title Page](#)[Abstract](#)[Introduction](#)[Conclusions](#)[References](#)[Tables](#)[Figures](#)[◀](#)[▶](#)[◀](#)[▶](#)[Back](#)[Close](#)[Full Screen / Esc](#)[Printer-friendly Version](#)[Interactive Discussion](#)

**Technical note: A
numerical test-bed
for ice nucleation**

R. J. Cotton et al.

**Fig. 3.** Empirically derived K_T for each chamber expansion.[Title Page](#)[Abstract](#)[Introduction](#)[Conclusions](#)[References](#)[Tables](#)[Figures](#)[◀](#)[▶](#)[◀](#)[▶](#)[Back](#)[Close](#)[Full Screen / Esc](#)[Printer-friendly Version](#)[Interactive Discussion](#)

Technical note: A numerical test-bed for ice nucleation

R. J. Cotton et al.

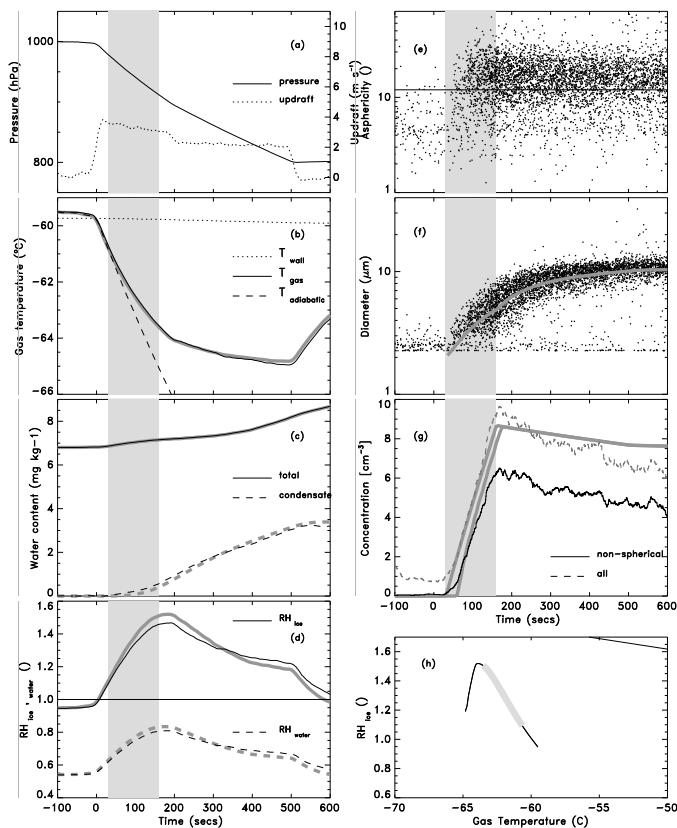


Fig. 4. Temperature regime I: Single nucleation mode. Model-observation comparison for Saharan dust (Expansion 45). The expansion starts at 0 s. Only one ice nucleation mode is observed with ice particles initiated between 30 and 160 s, as indicated by the light grey vertical shading. The two thick grey lines on panel (g) are the model concentration for all ice particles, and for ice particles with diameter greater than $3\ \mu\text{m}$ which is the SID size threshold.

Title Page

Abstract

Introduction

Conclusions

References

Tables

Figures

◀

▶

◀

▶

Back

Close

Full Screen / Esc

Printer-friendly Version

Interactive Discussion

Technical note: A numerical test-bed for ice nucleation

R. J. Cotton et al.

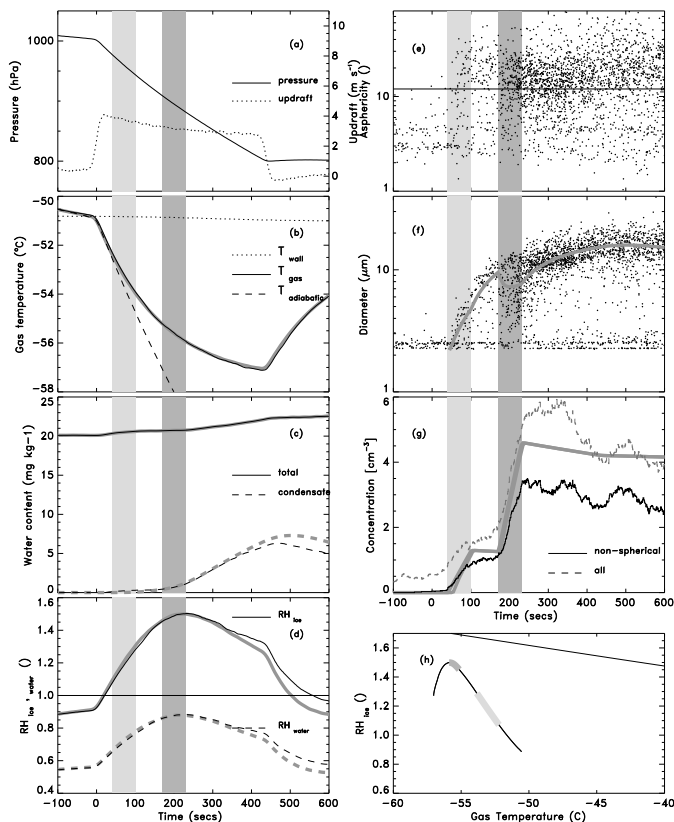


Fig. 5. Temperature regime II: Two ice nucleation modes. Model-observation comparison for Asian dust (Expansion 28). There are two distinct nucleation modes, with ice initiated between 40 and 100s and between 170 and 230s, as indicated by the light and dark grey vertical shading.

Title Page

Abstract

Introduction

Conclusions

References

Tables

Figures

◀

▶

◀

▶

Back

Close

Full Screen / Esc

Printer-friendly Version

Interactive Discussion

Technical note: A numerical test-bed for ice nucleation

R. J. Cotton et al.

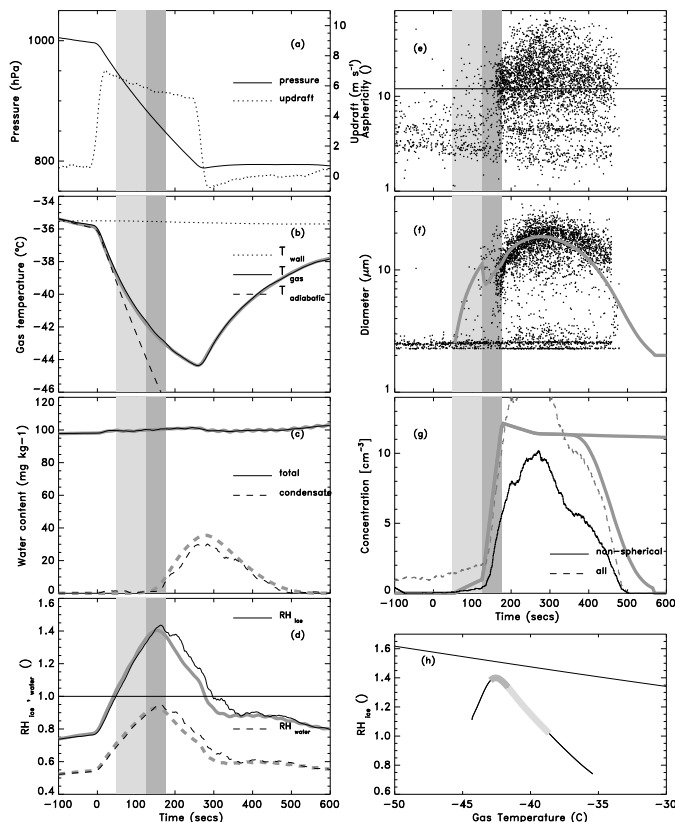


Fig. 6. Temperature regime III: Two nucleation modes. Model-observation comparison for Asian dust (Expansion 24). There are two nucleation modes, but they are not as distinct as for expansion 28. The two thick grey lines on panel (g) are the model concentration for all ice particles, and for ice particles with diameter greater than 3 μm which is the SID size threshold.

Title Page

Abstract

Introduction

Conclusions

References

Tables

Figures

◀

▶

◀

▶

Back

Close

Full Screen / Esc

Printer-friendly Version

Interactive Discussion

Technical note: A numerical test-bed for ice nucleation

R. J. Cotton et al.

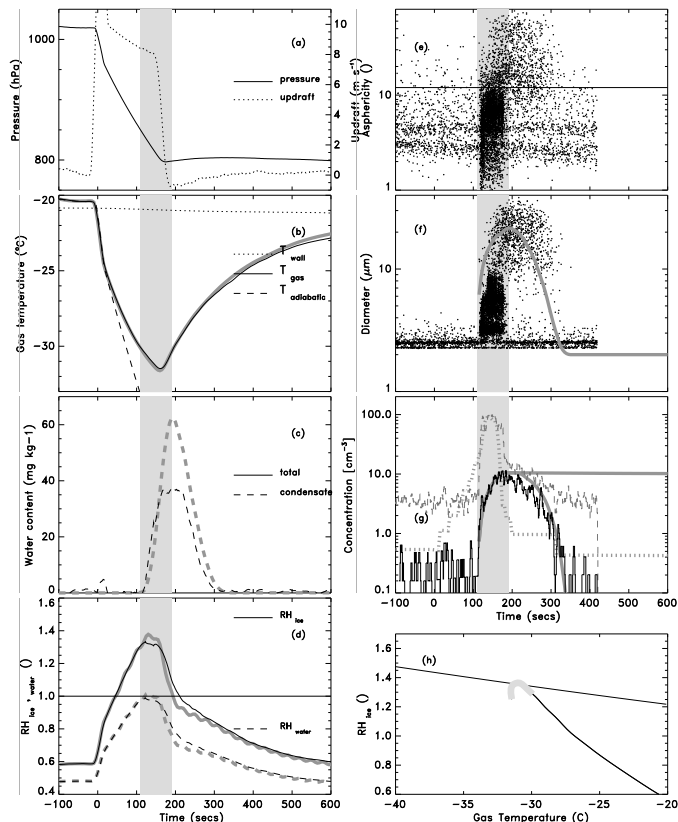


Fig. 7. Temperature regime IV: One nucleation mode, liquid water observed. Model-observation comparison for Asian dust (Expansion 19). Note that panel (g) now has a logarithmic scale in order to more clearly show both liquid and ice concentrations. The two thick grey lines on panel (g) are the model concentration for all ice particles, and for ice particles with diameter greater than $3\ \mu\text{m}$ which is the SID size threshold. The thick dashed grey line is the model drop concentration with diameter greater than $3\ \mu\text{m}$.

Title Page

Abstract

Introduction

Conclusions

References

Tables

Figures

◀

▶

◀

▶

Back

Close

Full Screen / Esc

Printer-friendly Version

Interactive Discussion

Technical note: A numerical test-bed for ice nucleation

R. J. Cotton et al.

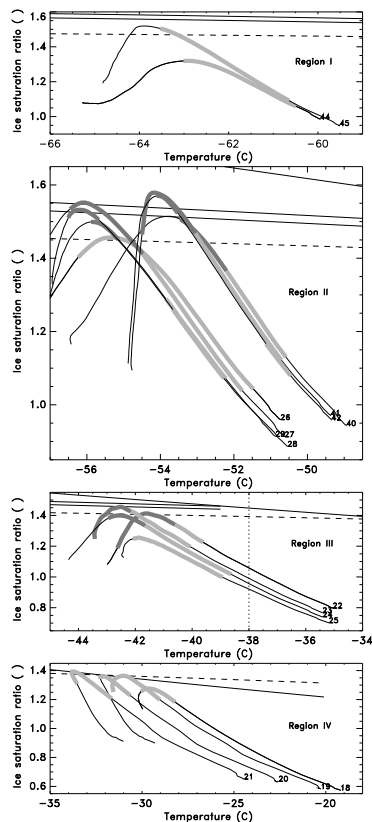


Fig. 8. Chamber temperature and humidity when ice nucleation occurs, indicated by the light- and dark-grey bands. Panels (a)–(d) cover the four temperature regimes I–IV defined in Table 1. The dashed line is immersion-freezing following Zuberi et al. (2002), and the two parallel lines are homogeneous freezing of aqueous ammonium sulphate following Koop et al. (2000).

Title Page

Abstract

Introduction

Conclusions

References

Tables

Figures

◀

▶

◀

▶

Back

Close

Full Screen / Esc

Printer-friendly Version

Interactive Discussion

**Technical note: A
numerical test-bed
for ice nucleation**

R. J. Cotton et al.

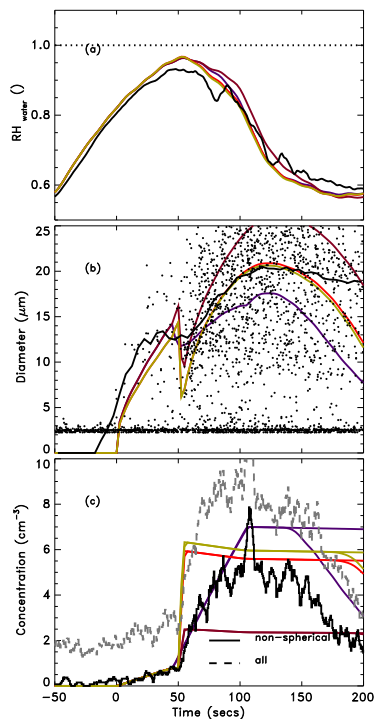


Fig. 9. Expansion 23 (Asian dust AD1) with initial chamber temperature -35°C , reaching -43°C when near water saturation. On each panel, the black line represents the observations (for the diameter, it is the median of all particles with a diameter greater than $4\ \mu\text{m}$). The purple line is for the model with both ice nucleation modes parametrised as before, by just inserting ice particles to match the SID observations. The brown, red and mustard lines are for models which assume homogeneous freezing for the second ice nucleation mode. The brown uses ammonium sulphate, the capacitance, $C=1$ and an aerosol subset fraction of 1.0. The red line uses ammonium sulphate, the capacitance, $C=0.8$ and an aerosol subset fraction of 0.4. The mustard line uses sulphuric acid, the capacitance, $C=0.8$ and an aerosol subset fraction of 0.4.

Title Page

Abstract

Introduction

Conclusions

References

Tables

Figures

◀

▶

◀

▶

Back

Close

Full Screen / Esc

Printer-friendly Version

Interactive Discussion

Technical note: A numerical test-bed for ice nucleation

R. J. Cotton et al.

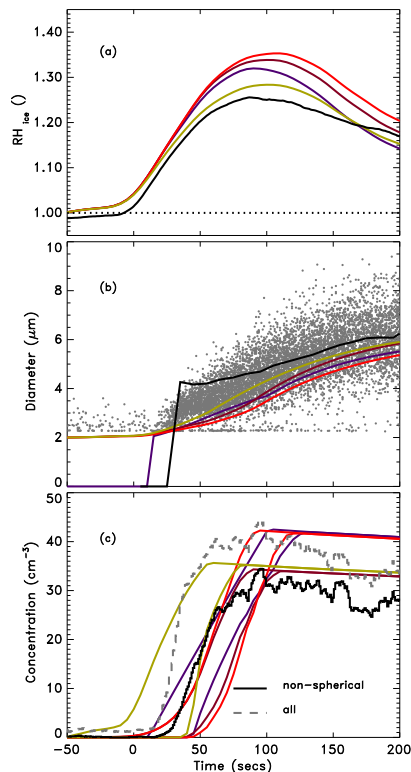


Fig. 10. Expansion 44 (Saharan dust SD2) with initial chamber temperature -60°C . On each panel, the black line represents the observations (for the diameter, it is the median of all particles with a diameter greater than $4\ \mu\text{m}$). The purple line is for the model with the ice nucleation modes parametrised as before, by just inserting ice particles to match the SID observations. The brown and red lines are for models which assume deposition nucleation following Meyers et al. (1992) and the mustard line using Eq. (6). On panel (c), the left-most line is the concentration of all ice crystals and the right-most line only ice crystals greater than $3\ \mu\text{m}$.

Title Page

Abstract

Introduction

Conclusions

References

Tables

Figures

◀

▶

◀

▶

Back

Close

Full Screen / Esc

Printer-friendly Version

Interactive Discussion